



Electrochemical cyclability mechanism for MnO₂ electrodes utilized as electrochemical supercapacitors

Weifeng Wei*, Xinwei Cui, Weixing Chen, Douglas G. Ivey

Department of Chemical and Materials Engineering, University of Alberta, Edmonton, Alberta, Canada T6G 2G6

ARTICLE INFO

Article history:

Received 2 September 2008

Received in revised form 10 October 2008

Accepted 13 October 2008

Available online 1 November 2008

Keywords:

Electrochemical supercapacitors

Manganese oxides

Electrochemical cyclability

Electrochemical impedance spectroscopy

Morphological and structural evolution

ABSTRACT

The electrochemical cyclability mechanism of nanocrystalline MnO₂ electrodes with rock salt-type and hexagonal ϵ -type structures was investigated to determine the relationship between physicochemical feature evolution and the corresponding electrochemical behaviour of MnO₂ electrodes. Rock salt MnO₂ and hexagonal ϵ -MnO₂ electrodes, with fibrous and porous morphologies, evolve into the antifluorite-type MnO₂ with a petal-shaped nanosheet structure after electrochemical cycling, similar to that observed in nanocrystalline antifluorite-type MnO₂ electrodes after electrochemical cycling. However, a different impedance response was observed for the rock salt MnO₂ and hexagonal ϵ -MnO₂ electrodes during the charge–discharge cycles, compared with the improved impedance response observed for the cycled antifluorite-type MnO₂. A dissolution–redemption mechanism is proposed to account for the impedance response of the MnO₂ electrodes with different morphologies and crystal structures.

© 2008 Elsevier B.V. All rights reserved.

1. Introduction

Electrochemical supercapacitors (ESs), with a combination of high power density and high energy density, can be used as a complementary energy-storage device along with a primary power source, such as a battery or a fuel cell, for power enhancement in short pulse applications [1]. For practical applications, an ES must fulfill the following technical requirements: high specific capacitance, long cycle life and high charge–discharge rate. Manganese oxides, characterized by low cost, abundance and environmentally friendly nature, have been extensively evaluated as active electrode materials for electrochemical supercapacitors [2–18] with the intention that manganese oxides will serve as a low-cost replacement for noble metal oxides, such as RuO₂ [19]. Hydrated manganese oxides exhibit specific capacitances within the 100–200 F g^{−1} range in alkali salt solutions, which are lower than those for RuO₂ ESs. Most of the research on manganese oxide ESs has focused on achieving the highest capacitance values by incorporating manganese oxides with well-designed electrode architectures such as carbon nanofoams, templated mesoporous carbon and nanotube assemblies, or adjusting synthesis conditions to obtain manganese oxides with desirable morphologies, defect chemistry (cation distributions and oxidation states) and crystal

structures [2–18]. However, only a couple of studies have dealt with the issue of electrochemical cycling stability in manganese oxide ESs [4,5,9].

For the amorphous and crystalline manganese oxides in the literature, the voltammetric capacitance has been observed to fade with increasing cycling numbers. It is noted that the extent of capacitance reduction is rather sensitive to the features of manganese oxide coatings such as morphology, crystal chemistry and even coating thickness, so that very scattered results have been reported. For instance, Toupin et al. reported essentially no capacity fading after 1000 cycles for a thick coating electrode (>100 μm) at a slow scan rate of 2 mV s^{−1} [6]. More recently, Brousse et al. reported that long-term cycling behavior with stable performance (>100,000) was realized in a carbon–MnO₂ hybrid electrochemical supercapacitor cells [20]. In contrast, Pang and Anderson reported that there was more than 10% capacity loss after 1500 cycles at a scan rate of 50 mV s^{−1} for thin MnO₂ electrodes (<15 $\mu\text{g cm}^{-2}$) fabricated by a sol–gel process [4,5]. Hsieh et al. also reported a wide range of capacity fading for thick MnO₂ electrodes, ranging from 5 to 30% in 1000 cycles, which is rather sensitive to the scan rate and binder content [21].

Until now, two mechanisms have been proposed to explain the capacitance fading behavior. The first mechanism involves partial dissolution of the MnO₂ films into the electrolyte during cycling, i.e., active electrode material loss, which has been confirmed by chemical analysis of Mn content in the electrolytes [4,5,9]. However, no impedance results have been obtained to further evaluate

* Corresponding author. Tel.: +1 780 492 8849; fax: +1 780 492 2881.
E-mail address: weifeng@ualberta.ca (W. Wei).

the electrochemical behaviour of cycled MnO_2 films. More recently, Hsieh et al. reported that the dissolution amounts of their thick MnO_2 electrodes (<0.5%) are too low to account for the extent of capacitance fading (5–30%) [21]. A second mechanism was therefore proposed: the accelerated fading can be mainly attributed to gradual mechanical failure of the electrode materials caused by cyclic volumetric variations of the oxide particles upon cycling. The failure leads to increasingly deteriorating electrical contact among the constituent particles within the electrode, which has been confirmed by an increase in impedance for the cycled electrode [21]. Both proposed mechanisms imply that the electrochemical cyclability is closely related to physicochemical feature evolution in MnO_2 electrodes during charge–discharge cycles, such as morphological, chemical and structural changes. However, the relationship between physicochemical feature evolution and corresponding electrochemical impedance response of MnO_2 electrodes has not been clarified.

In our recent investigations, MnO_2 nanocrystals with three types of crystal structures, including hexagonal ε - MnO_2 , defective rock salt MnO_2 and defective antiferroite MnO_2 , were synthesized by introducing complexing agents into the electrodeposition solutions [22,23]. During electrochemical charge–discharge cycles, improved electrochemical impedance response was found for MnO_2 electrodes with a defective antiferroite structure [24]. In the high frequency region, the charge transfer resistance is observed to decrease from $0.26 \Omega \text{ cm}^2$ (as-prepared) to $0.08 \Omega \text{ cm}^2$ for the electrode after 100 cycles. The knee frequency (lower limit of the charge transfer region) was raised from 501 Hz (as-prepared) to 1.26 kHz (100 cycles), exhibiting improved electrochemical response. At low frequencies, the capacitor response frequency, $f_{\phi=-45^\circ}$, shifts from 1 to 6 Hz, and the response time of the capacitor is reduced from 1 s (as prepared) to ~ 0.2 s. This distinct electrochemical behaviour is attributed to morphological and structural evolution from equiaxed oxide nanocrystals to petal-shaped, single-crystal nanosheets [24]. It is apparent that the improved electrochemical impedance response cannot be explained by a dissolution mechanism or a mechanical failure mechanism induced by cyclic volumetric variation. The physicochemical feature evolution during charge–discharge needs to be further correlated to the electrochemical cyclability of the MnO_2 electrodes.

Inspired by these considerations, the present study extends our initial study to examine the relationship between physicochemical feature evolution and the corresponding electrochemical behaviour of MnO_2 electrodes with hexagonal ε - MnO_2 and defective rock salt structures. Morphological, chemical and structural information is obtained using scanning electron microscopy (SEM), X-ray photoelectron spectroscopy (XPS) and transmission electron microscopy (TEM). Electrochemical characterization is performed with cyclic voltammetry (CV) and electrochemical impedance spectroscopy (EIS). It is expected that this work may provide new insights on the electrochemical cyclability mechanisms of manganese oxide ESs.

2. Experimental procedure

2.1. Materials synthesis

Nanocrystalline MnO_2 coatings were deposited from 0.3 M MnSO_4 solutions, with and without 0.2 M ethylenediaminetetraacetic acid (EDTA) disodium, by anodic electrodeposition, as described previously [22–25]. The deposition current density, electrolyte pH value and electrolyte temperature were adjusted to be 100 mA cm^{-2} , 7.0 and 70°C , respectively. During electrodeposition, agitation was introduced with a magnetically driven Teflon[®] coated

stirring bar at a speed of 300 rpm. The mass of the MnO_2 nanocrystals on the Pt electrodes was controlled to be 0.20 – 0.25 mg cm^{-2} of the electrode surface area. After electrodeposition, the working electrodes were rinsed with deionized water, dried at 100°C for 60 min in air and then stored in a vacuum desiccator before further electrochemical testing and analysis.

2.2. Materials characterization

The morphology and chemistry of as-prepared and cycled electrodes were analyzed in a JAMP 9500F field emission scanning Auger microprobe (FE-SAM). Chemical state analysis was carried out by X-ray photoelectron spectroscopy (XPS) using a Kratos AXIS Ultra X-ray photoelectron spectrometer. A monochromatic Al source, operating at 210 W with a pass energy of 20 eV and a step of 0.1 eV, was utilized. All XPS spectra were corrected using the C 1 s line at 284.6 eV. Curve fitting and background subtraction were accomplished by using Casa XPS Version 2.3.13 software. The crystal structure and morphology of the oxides were investigated using a JEOL 2010 transmission electron microscope (TEM) equipped with a Noran ultra-thin window (UTW) X-ray detector.

2.3. Electrochemical behavior

Electrochemical behavior was investigated with a Gamry PC4/750 potentiostat/galvanostat under cyclic voltammetry (CV) and potentiostatic electrochemical impedance spectroscopy (EIS) modes in an electrolyte containing 0.5 M Na_2SO_4 . A saturated calomel electrode (SCE) was used as the reference and all potentials quoted are with respect to it. Cyclic voltammograms were recorded between -0.1 and 0.8 V vs. SCE at 100 mV s^{-1} . EIS measurements were conducted on MnO_2 electrodes cycled for various cycle numbers in constant voltage mode (0.2 V vs. SCE) by sweeping frequencies from 100 kHz to 10 mHz at an amplitude of 5 mV. The Mn content in the 0.5 M Na_2SO_4 electrolyte after electrochemical cycling was determined using a VARIAN 220 FS atomic absorption spectrophotometer (AAS).

3. Results and discussion

3.1. Morphology and crystal structure of as-prepared MnO_2 electrodes

The morphology and crystal structure of the as-prepared MnO_2 coatings obtained from 0.3 M MnSO_4 solutions, with and without 0.2 M EDTA addition, were analyzed using SEM and TEM. Plan view secondary electron (SE) images, shown in Fig. 1a and c, indicate that both oxides are composed of nano-scale fibers entangled with one another. The dark field (DF) TEM micrographs in Fig. 1b and d reveal that the nano-scale fibers are not individual oxide crystals, but are composed of equiaxed oxide nanocrystals with a diameter less than 10 nm. Corresponding selected area electron diffraction (SAED) patterns taken from these two oxide coatings are shown in the insets of Fig. 1b and d. Continuous ring patterns also confirm their nanocrystalline nature. The d -spacings measured from the SAED pattern for the MnO_2 prepared from the EDTA-containing solution (Fig. 1b) are consistent with face-centered cubic (FCC) MnO (JCPDS Card No. 07-0230) with a space group of $Fm\bar{3}m$, which is in agreement with our previous study [22,23]. The diffracted rings are indexed to be (1 1 1), (2 0 0), (2 2 0), (3 1 1) and (2 2 2), respectively, shown in the inset of Fig. 1b. The diffraction data, obtained from the SAED pattern for the Mn oxide coating prepared from the EDTA-free solution, is consistent with that of hexagonal ε - MnO_2 (JCPDS Card No. 30-0820) with a space group of $P6_3/mmc$. The diffracted rings are indexed to be (10 $\bar{1}$ 0), (10 $\bar{1}$ 1), (10 $\bar{1}$ 2) and (11 $\bar{2}$ 1),

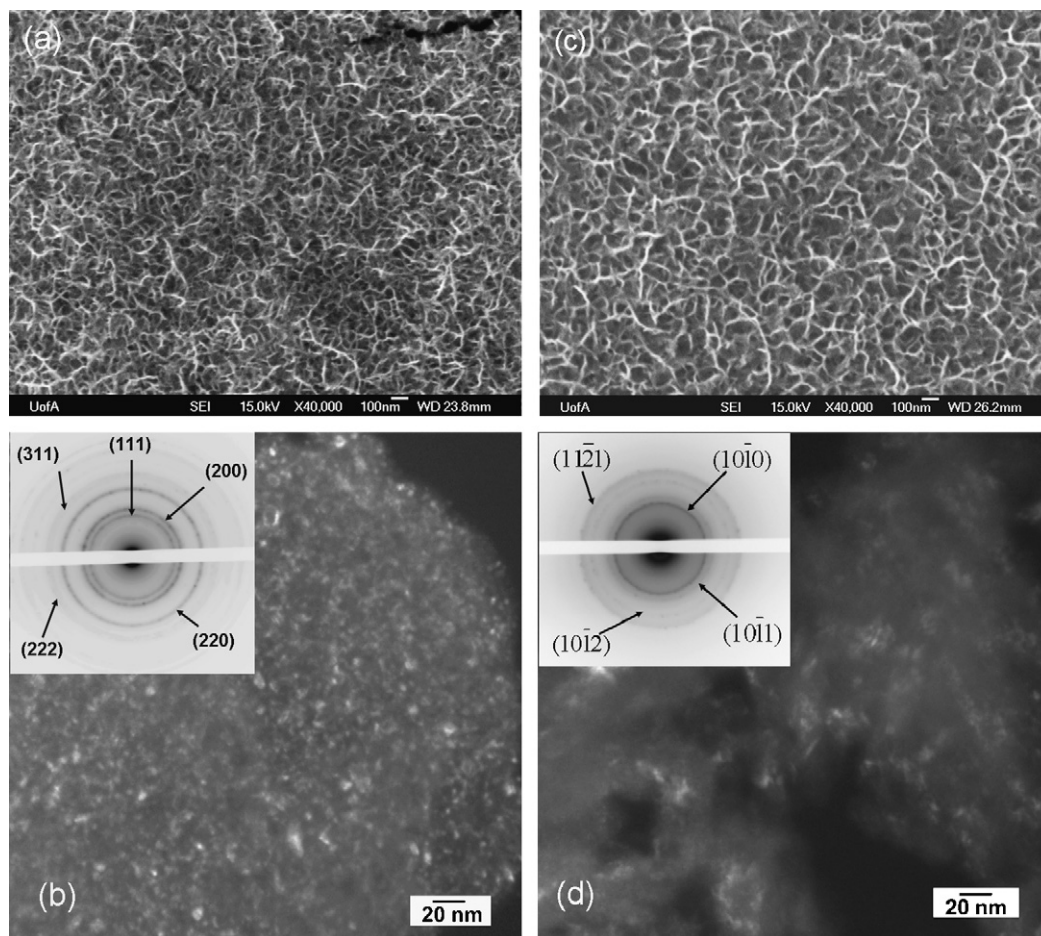


Fig. 1. (a) SEM SE micrograph and (b) TEM DF micrograph with SAED pattern (inset) taken from as prepared rock salt MnO_2 ; (c) SEM SE micrograph and (d) TEM DF micrograph with SAED pattern (inset) taken from as prepared hexagonal $\epsilon\text{-MnO}_2$.

shown in the inset of Fig. 1d. This structure can be described as a NiAs unit cell, with Mn^{4+} cations randomly occupying 50% of the octahedral positions of the hexagonal close packed (hcp) oxygen sublattice.

3.2. Chemical states of as-prepared MnO_2 electrodes

Chemical state information for the as-prepared MnO_2 coatings with rock salt and hexagonal structures was studied using XPS. The oxidation states for the Mn cations were determined by analyzing the Mn 3s XPS spectra. The doublet Mn 3s peaks are the result of parallel spin coupling between electrons in the 3s and 3d orbitals. The oxidation states for Mn are closely related to the 3s peak splitting widths. When the valence of the Mn cations decreases, i.e., more electrons exist in the 3d orbitals, the splitting width increases [26–28]. Fig. 2a shows Mn 3s spectra for these two oxides. Based on an approximately linear relationship between the splitting width (ΔE) and the Mn oxidation state [26,28], the Mn cations in these two oxides have an average valence close to +4. Fig. 2b shows the corresponding XPS O 1s spectra. The O 1s spectrum can be deconvoluted into three components, including oxide (O–Mn–O), hydroxide (Mn–O–H) and water content (H–O–H) (Fig. 2b), which may also be used to estimate the valence of Mn cations [29]. Considering that the Mn oxide electrodes were prepared based on electro-oxidation of Mn^{2+} ions on the anode surfaces using anodic electrodeposition, the formation of $\text{Mn}(\text{OH})_2$ is not favorable thermodynamically, so the hydroxide in the Mn oxide

electrodes is probably in the form of MnOOH . Based on Fig. 2b, the contents of MnO_2 and MnOOH were determined to be 67.3% and 22.1% for hexagonal $\epsilon\text{-MnO}_2$ and 65.7% and 20.2% for rock salt MnO_2 , respectively. Therefore, the average valences of Mn cations in the hexagonal $\epsilon\text{-MnO}_2$ and rock salt MnO_2 are in the range of 3.7–3.8.

3.3. Electrochemical properties of MnO_2 electrodes

The electrochemical properties of the two oxide coatings were first evaluated using CV scans in a 0.5 M Na_2SO_4 solution. Fig. 3a and b shows the cyclic voltammograms obtained from the two oxide coatings at a scan rate of 100 mV s^{-1} for up to 500 cycles. The voltammetric curves are observed to shrink with increasing cycling number. The specific capacitance C (F g^{-1}) of the MnO_2 electrodes, based on the cyclic voltammograms (Fig. 3), was determined by integrating each cyclic voltammogram to obtain the voltammetric charge (Q). Then Q was divided by the mass of the active materials in the electrodes (m) and the width of the potential window ΔE . It is noted that, after 500 cycles at 100 mV s^{-1} , the reduction in specific capacitance is determined to be 27% of the original value (152 F g^{-1}) for the defective rock salt MnO_2 , while the capacitance fading is about 38% of the original value (91 F g^{-1}) for the hexagonal $\epsilon\text{-MnO}_2$ electrode. The capacitance values for rock salt MnO_2 and $\epsilon\text{-MnO}_2$ are comparable to those in the literature considering the high scan rate applied (100 mV s^{-1}). The capacitance differences in these two Mn oxides can be explained

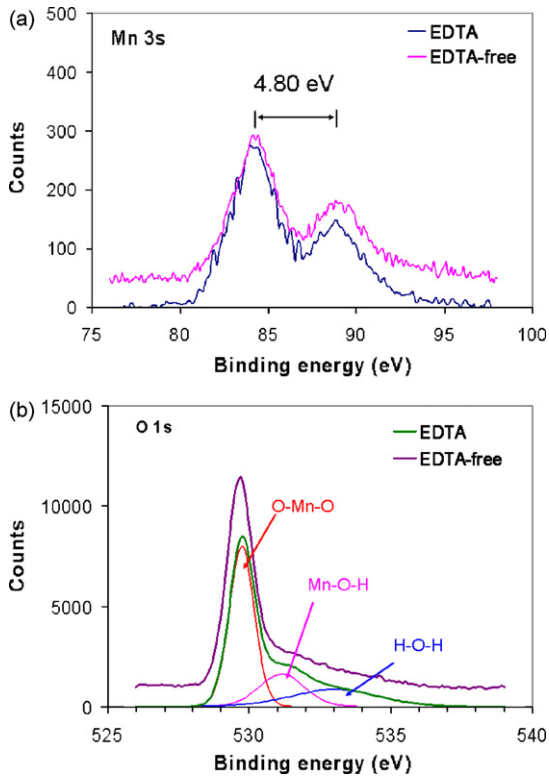


Fig. 2. Mn 3s (a) and O 1s (b) XPS spectra from the as-prepared rock salt MnO_2 and hexagonal $\epsilon\text{-MnO}_2$ electrodes.

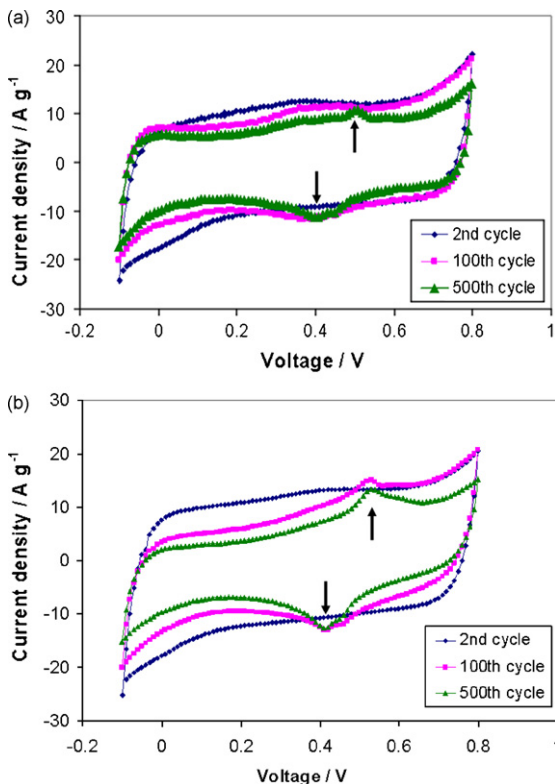


Fig. 3. Cyclic voltammograms taken from MnO_2 electrodes cycled at 100 mV s^{-1} for up to 500 cycles: (a) rock salt MnO_2 and (b) hexagonal $\epsilon\text{-MnO}_2$.

Table 1

Dissolved Mn content in the 0.5 M NaSO_4 electrolyte after 500 cycles at 100 mV s^{-1} .

Electrode	Measured Mn content in 50 ml electrolyte (ppm)	Dissolved percentage of MnO_2 electrode (%)
Rock salt-type MnO_2	0.54	9.4
Hexagonal $\epsilon\text{-MnO}_2$	0.61	10.2

in terms of the crystal chemistry, as discussed previously [23]. The electrolyte solutions after electrochemical cycling were analyzed for Mn content using AAS. Manganese was indeed detected in the electrolyte solutions, however, the amount in solution is around 10% for the two oxide electrodes (Table 1). The dissolution amounts for the MnO_2 electrodes are too low to account for the extent of capacitance losses in both the rock salt MnO_2 and $\epsilon\text{-MnO}_2$ electrodes.

The cyclic voltammograms initially exhibit essentially rectangular-shaped profiles, characteristic of good capacitive behavior. With increasing cycle number, the voltammetric curves exhibit broad anodic and cathodic peaks centered at 0.53 and 0.40 V vs. SCE, shown by the black arrows in Fig. 3a and b. It has been well established that the Faradaic reactions occurring on the surface and in the bulk of the materials are the major charge storage mechanisms for MnO_2 materials. The surface Faradaic reaction involves the surface adsorption of electrolyte cations ($\text{C}^+ = \text{Li}^+, \text{Na}^+$ and K^+) on the manganese oxides [2,3,29]:



The bulk Faradaic reaction relies on the intercalation or deintercalation of H^+ or alkaline metal cations in the bulk of the manganese oxides [4,29]:



The redox reaction peaks (shown as arrows in Fig. 3a and b) can be attributed to cation deintercalation upon oxidation and cation intercalation upon reduction [30]. The redox reaction peaks were observed to be more prominent with increasing cycle number, which means that the partial cation intercalation/deintercalation reactions contribute more in the total capacitance in both the rock salt MnO_2 and $\epsilon\text{-MnO}_2$ electrodes after electrochemical cycling. In order to understand this trend, morphological and structural analysis on cycled MnO_2 electrodes is needed.

3.4. Morphology and crystal structure of cycled MnO_2 electrodes

TEM micrographs and corresponding SAED patterns, shown in Fig. 4, were taken from the rock salt MnO_2 and $\epsilon\text{-MnO}_2$ electrodes after 500 cycles at 100 mV s^{-1} . From the bright field (BF) TEM images (Fig. 4a and d), a fibrous morphology, composed of equiaxed nanocrystals, evolves into petal-shaped thin nanosheets in the cycled MnO_2 electrodes. SAED ring patterns taken from the overall areas (both the equiaxed nanocrystals and petal-shaped features) are shown in Fig. 4b and e. These two SAED patterns exhibit antifluorite-type crystallographic features, which are consistent with those taken from cycled antifluorite-type MnO_2 in a previous study [24]. The SAED patterns in Fig. 4c and f, taken from the petal-shaped features (the circled areas in Fig. 4a and d), confirm that each thin oxide sheet is actually a single crystal with the same crystal structure, but different orientation. After careful examination of the SAED ring patterns (Fig. 4b and e), the d -spacing sequences for the first four diffraction rings of the cycled MnO_2 electrodes are 0.245, 0.213, 0.145 and 0.121 nm, which are also in agreement with those from cycled antifluorite-type MnO_2 electrode in a previous study

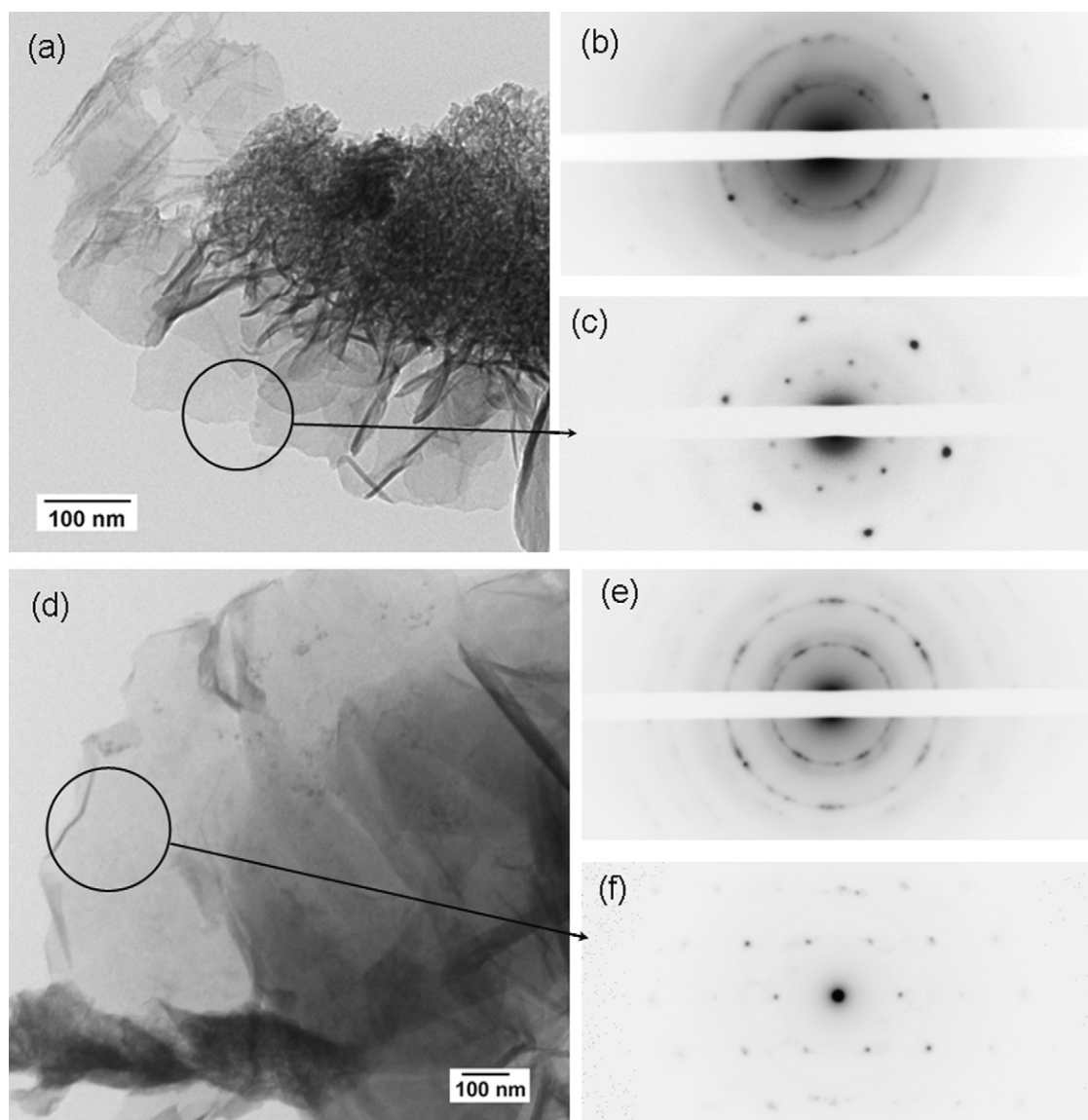


Fig. 4. Morphology and crystal structure for MnO_2 electrodes after 500 cycles at 100 mV s^{-1} . (a) TEM BF micrograph for rock salt MnO_2 ; (b) SAED pattern taken from the overall area for rock salt MnO_2 ; (c) SAED pattern taken from the petal-shaped feature for rock salt MnO_2 . (d) TEM BF micrograph for hexagonal ϵ - MnO_2 ; (e) SAED pattern taken from the overall area for hexagonal ϵ - MnO_2 ; (f) SAED pattern taken from the petal-shaped feature for hexagonal ϵ - MnO_2 .

[24]. The unit cells for the cycled MnO_2 electrodes have decreased in size, i.e., are denser, when compared with those for as-prepared antifluorite-type MnO_2 [22].

It is noted that morphological and structural evolution after electrochemical cycling has been found in other MnO_2 polymorphs. For instance, similar surface morphology evolution, from equiaxed to petal-shaped features, has also been detected for thin film MnO_2 electrodes after cycling in previous studies [5,31]. Dai et al. reported the structural transformation from distorted spinel Mn_3O_4 to layered structure birnessite after cycling in aqueous Na_2SO_4 [31]. In contrast, Athouel et al. reported a crystallinity loss but no structural transformation for crystallized Mg-doped sodium birnessite-type manganese dioxide electrodes after electrochemical cycling [32]. It has been confirmed that this physicochemical feature evolution in MnO_2 electrodes has significant effects on the electrochemical behaviour [5,31,32]. In this work, EIS is applied to further understand the relationship between physicochemical feature evolution and corresponding electrochemical response of MnO_2 electrodes.

3.5. Electrochemical impedance response of MnO_2 electrodes during electrochemical cycling

The impedance data for defective rock salt MnO_2 and hexagonal ϵ - MnO_2 during electrochemical cycling is shown in Figs. 5 and 6. Nyquist plots in Figs. 5a and b and 6a and b show that each impedance spectrum can be generally divided into three regions corresponding to three processes: a very small arc in the very high frequency range (double layer process), a depressed semi-circle in the high frequency range (charge transfer process) and a straight line at low frequencies (electrolyte diffusion process). With increasing cycle number, no obvious differences are observed for the double layer process in the insets of Figs. 5a and 6a. For the charge transfer process, the plots for rock salt MnO_2 shift along the real axis to higher resistance with increasing cycle number (the inset of Fig. 5a), while the plots for hexagonal ϵ - MnO_2 remain almost the same (the inset of Fig. 6a). From the admittance spectra in Figs. 5b and 6b, the lower limit of the high frequency region (charge

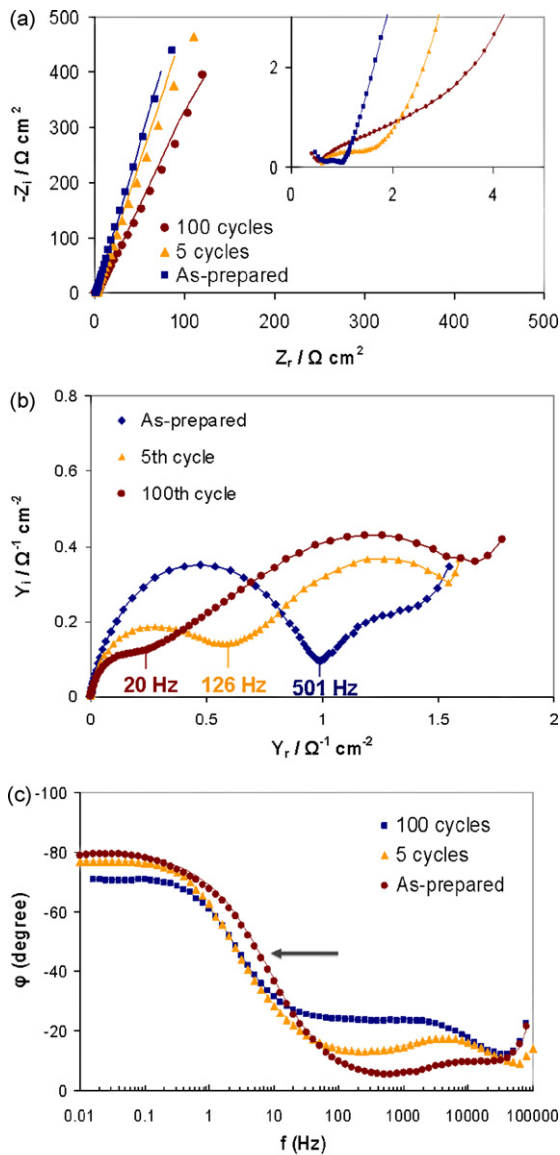


Fig. 5. (a) Complex-plane impedance plots; (b) admittance plots; and (c) phase frequency dependency plots for the rock salt-type MnO_2 electrode after various cycling numbers at 100 mV s^{-1} . The solid lines represent data fit to the equivalent circuit in Fig. 7.

transfer process) is characterized by a knee frequency. The knee frequency for rock salt MnO_2 is reduced from 501 Hz (as-prepared) to 20 Hz (100 cycles), exhibiting degraded electrochemical response. The knee frequency for hexagonal $\varepsilon\text{-MnO}_2$ remains within the range of 376–389 Hz with increasing cycle number. At low frequencies (Figs. 5a and 6a), straight lines with various slopes are present in the impedance plots. The frequency where $\phi = -45^\circ$ ($f_{\phi=-45^\circ}$) is

Table 2

Selected data obtained from fitting the experimental impedance data to the equivalent circuit in Fig. 7.

	Rock salt-type MnO_2			Hexagonal $\varepsilon\text{-MnO}_2$		
	As-prepared	5 cycles	100 cycles	As-prepared	5 cycles	100 cycles
R_1 ($\Omega \text{ cm}^2$)	0.36(2)	0.38(1)	0.29(2)	0.14(0)	0.10(1)	0.13(0)
R_2 ($\Omega \text{ cm}^2$)	0.38(1)	0.60(2)	1.12(2)	0.28(1)	0.26(0)	0.26(1)
R_3 ($\Omega \text{ cm}^2$)	0.09(1)	0.16(1)	0.65(2)	1.02(2)	0.78(1)	0.71(2)
f_{knee} (Hz)	501	126	20	389	376	389
$f_{\phi=-45^\circ}$ (Hz)	5.6	3.3	3.0	3.0	3.3	3.3

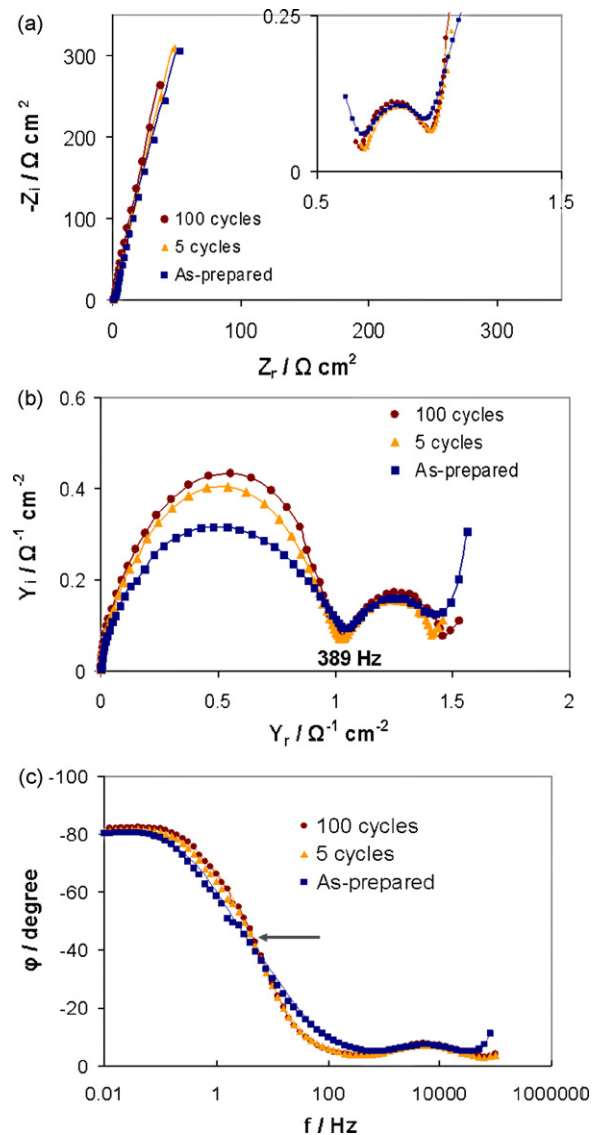


Fig. 6. (a) Complex-plane impedance plots; (b) admittance plots; and (c) phase frequency dependency plots for the hexagonal $\varepsilon\text{-MnO}_2$ electrode after various cycling numbers at 100 mV s^{-1} . The solid lines represent data fit to the equivalent circuit in Fig. 7.

the frequency response corresponding to ideally capacitive behavior (capacitor response frequency) [33]. After cycling at 100 mV s^{-1} , $f_{\phi=-45^\circ}$ shifts from 5.6 to 3 Hz for rock salt MnO_2 (Fig. 5c), while $f_{\phi=-45^\circ}$ for hexagonal $\varepsilon\text{-MnO}_2$ is maintained around 3 Hz (Fig. 6c). The knee frequency and the capacitor response frequency are tabulated in Table 2.

In order to obtain quantitative information from EIS spectra, the impedance data can be modeled assuming three major pro-

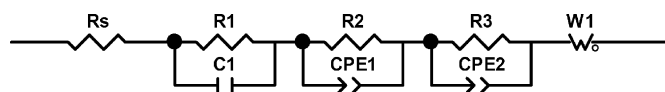


Fig. 7. An equivalent circuit for modeling the experimental impedance spectra obtained from the MnO_2 electrodes with different morphologies and crystal structures.

cesses in the entire frequency range (Fig. 7). Here, R_s is the solution resistance. R_1 and C_1 in this model are the contact resistance and capacitance between oxide nanocrystals as well as those at the interface of oxide materials and Pt current collectors [34]. R_2 and a constant phase element one (CPE_1) are used to account for the charge transfer process (the depressed semi-circle in each spectrum) on the surface of the electrode in contact with the electrolyte. A circuit ($R_3\text{CPE}_2$) W_1 is used to fit the diffusion process of the electrolyte in the porous electrode at low frequencies. The fitted data is consistent with the experimental data throughout the entire frequency range, shown as the solid curves in Figs. 5 and 6. Selected data obtained from fitting the experimental impedance data to the equivalent circuit is summarized in Table 2.

For the high frequency range, the charge transfer resistance increases from 0.38Ω (as-prepared) to 1.12Ω for the rock salt MnO_2 electrode after 100 cycles. This is further confirmed by the reduced knee frequency observed in the cycled electrodes. For hexagonal $\epsilon\text{-MnO}_2$, the charge transfer resistance values do not change with electrochemical cycling. For the low frequency range, the impedance is dominated by the electrolyte diffusion process. Normally, a higher slope for the impedance line means a lower diffusive resistance for the electrolyte in the electrode. It is apparent that the slope of the impedance line decreases with cycle number for rock salt MnO_2 . This implies that cation intercalation/deintercalation is hindered in the cycled electrodes, which is

supported by the higher resistance values and degraded capacitor response frequency in Table 2. For hexagonal $\epsilon\text{-MnO}_2$, however, similar slopes are observed for the impedance lines with increasing cycle number, which implies the diffusive resistance of electrolyte in the electrode is not affected by the electrochemical cycling.

3.6. Electrochemical cyclability mechanism

Even though antifluorite MnO_2 [24], rock salt MnO_2 and hexagonal $\epsilon\text{-MnO}_2$ evolve into the same antifluorite-type MnO_2 with a petal-shaped nanosheet structure after electrochemical cycling improved impedance response for the whole frequency range is only observed for the antifluorite MnO_2 electrodes during the charge–discharge cycles. This suggests that other factors, such as the morphology and structure of MnO_2 electrodes before electrochemical cycling, may influence the subsequent impedance response during the charge–discharge process. In our recent investigation, it was suggested that the morphological and structural evolution from equiaxed nanocrystals to petal-shaped, single-crystal nanosheets follows a dissolution–redeposition mechanism [24]. Considering the inhomogeneous nature of the MnO_2 electrodes, the dissolution process should be sensitive to their morphologies and crystallization degrees. A schematic model is proposed in Fig. 8 to demonstrate how inhomogeneous dissolution and redeposition in MnO_2 electrodes with different morphologies and structures affect the electrochemical behaviour.

For antifluorite-type MnO_2 , prepared from a citrate-containing 0.3 M MnSO_4 solution, a dense layer is present, consisting of agglomerated tiny oxide particles [23,24]. As the applied potential is scanned from 0.8 V to -0.1 V vs. SCE, the equiaxed MnO_2 nanocrystals will be reduced and some will be dissolved into the electrolyte as Mn^{2+} cations [24]. Since the oxide layer is densely

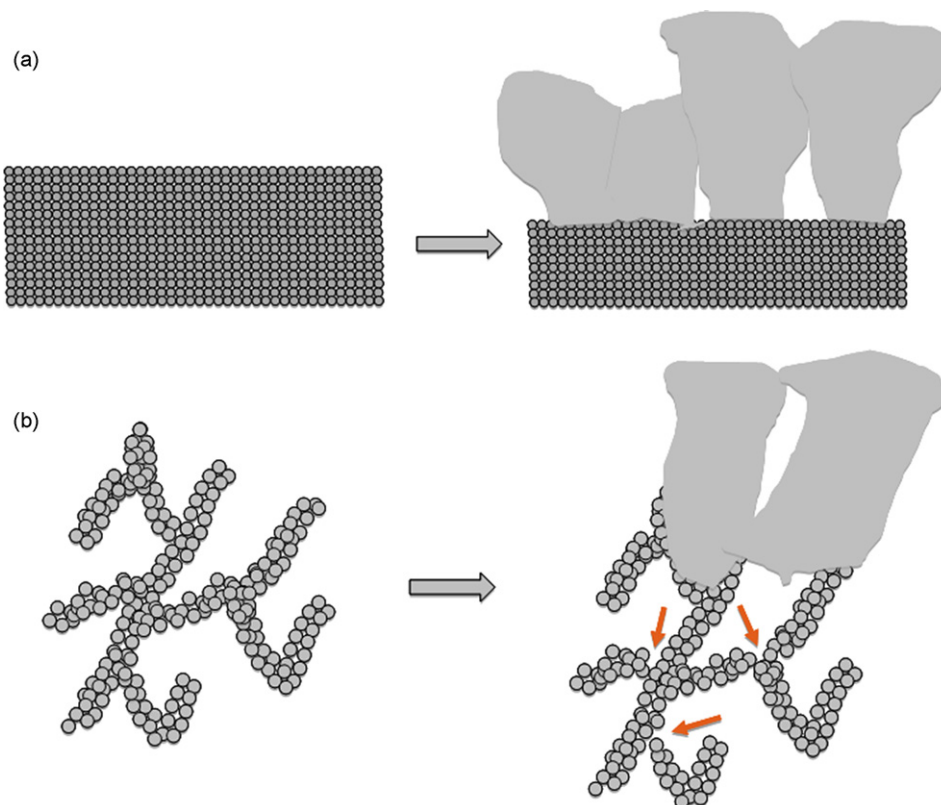


Fig. 8. A schematic representation of the dissolution–redeposition mechanism for (a) dense antifluorite-type MnO_2 and (b) porous and fibrous rock salt MnO_2 and hexagonal $\epsilon\text{-MnO}_2$.

packed, the dissolution process only occurs for the outermost sub-layer of the MnO_2 electrode. During forward cycling, some of the dissolved Mn^{2+} cations will be re-oxidized to MnO_2 and deposit as petal-shaped nanosheets on the MnO_2 electrode surface, as shown in Fig. 8a. In this case, the electrical contacts, including interparticle and particle/Pt current collector contacts, will not be affected by the dissolution process. Meanwhile, the petal-shaped nanosheets induced by the redeposition process not only improve the electrical conductivity by reducing the interparticle contact resistance, but facilitate electrolyte transport. This may account for the improved impedance response for antiferrotype MnO_2 electrodes during charge–discharge cycles.

The dissolution process in the rock salt MnO_2 and hexagonal ε - MnO_2 electrodes is rather different due to their porous and fibrous nature. It has been confirmed in Fig. 1 that these two oxides are actually nano-scale fibrous networks. The entangled nano-scale fibers are composed of equiaxed oxide nanocrystals with a diameter less than 10 nm. As the applied potential is scanned from 0.8 V to -0.1 V vs. SCE, the dissolution process may occur preferentially at high energy sites such as interparticle interfaces, fiber/fiber connection areas and active material/Pt current collector contact areas. With increasing cycle number, more MnO_2 will be dissolved and redeposited as petal-shaped nanosheets on the MnO_2 electrode surface. This leads to the weakening or even fracture of the interparticle interfaces, fiber/fiber connection areas and MnO_2 /Pt contact areas, as shown by the orange arrows in Fig. 8b. A direct consequence is increasingly deteriorating electrical contacts between the oxide particles even though the dissolution amount is small. This may explain the difference between the dissolution amounts for MnO_2 electrodes and the capacity reductions. The improvement in the impedance response induced by the petal-shaped nanosheets is offset by the poorer electrical contact between the oxide particles, so that similar impedance responses are observed for as prepared and cycled hexagonal ε - MnO_2 electrodes and degraded behavior, relative to as prepared samples, is observed for cycled rock salt MnO_2 electrodes.

From the voltammetric curves in Fig. 3a and b and the calculated capacitance data, it is noted that rock salt MnO_2 has better cyclability when compared with hexagonal ε - MnO_2 , which is in contradiction with the EIS results. One possible explanation for the discrepancy between the capacitance loss and EIS results is that the extent of morphological and structural evolution may be different for rock salt MnO_2 and hexagonal ε - MnO_2 . If the extent of morphological and structural evolution for the cycled hexagonal ε - MnO_2 is higher, i.e., more petal-shaped features, the specific surface area will decrease. Thus, the electrochemical frequency response is higher but the specific capacitance is lower because of low surface area utilization. To uncover the underlying reasons for this phenomenon, further investigation is required to obtain quantitative information on the morphological and structural evolution for MnO_2 electrodes.

4. Conclusions

The electrochemical cyclability of nanocrystalline MnO_2 electrodes with rock salt-type and hexagonal ε -type structures was investigated with cyclic voltammetry and electrochemical impedance spectroscopy. The main objective was to determine the relationship between physicochemical feature evolution and the corresponding electrochemical behaviour of MnO_2 electrodes with

different morphologies and crystal structures. Both rock salt MnO_2 and hexagonal ε - MnO_2 evolve into antiferrotype MnO_2 with a petal-shaped nanosheet structure after electrochemical cycling, similar to that observed in nanocrystalline antiferrotype MnO_2 electrodes after electrochemical cycling. However, no improvement in the impedance response was observed in the rock salt MnO_2 and hexagonal ε - MnO_2 electrodes during charge–discharge cycles, which is inconsistent with that observed in the cycled antiferrotype MnO_2 [23]. A dissolution–redeposition mechanism is proposed to account for different impedance response of MnO_2 electrodes with different morphologies and crystal structures in terms of morphological and structural evolution.

Acknowledgments

The authors would like to acknowledge funding contributions from the Natural Sciences and Engineering Research Council (NSERC) of Canada and Versa Power Systems (VPS). The authors are also grateful to the Alberta Centre for Surface Engineering and Science (ACES) for providing XPS and SEM analysis.

References

- [1] B.E. Conway, *Electrochemical Supercapacitors, Scientific Fundamentals and Technological applications*, Kluwer Academic/Plenum Press, New York, 1999.
- [2] H.Y. Lee, V. Manivannan, J.B. Goodenough, C.R. Acad. Sci. Paris, t2, Série II c 2 (1999) 565.
- [3] H.Y. Lee, J.B. Goodenough, J. Solid State Chem. 144 (1999) 220.
- [4] S.C. Pang, M.A. Anderson, T.W. Chapman, J. Electrochem. Soc. 147 (2000) 444.
- [5] S.C. Pang, M.A. Anderson, J. Mater. Res. 15 (2000) 2096.
- [6] M. Toupin, T. Brousse, D. Belanger, Chem. Mater. 14 (2002) 3946.
- [7] C.C. Hu, T.W. Tsou, Electrochem. Commun. 4 (2002) 105.
- [8] C.C. Hu, C.C. Wang, J. Electrochem. Soc. 150 (2003) A1079.
- [9] R.N. Reddy, R.G. Reddy, J. Power Sources 124 (2003) 330.
- [10] J.K. Chang, W.T. Tsai, J. Electrochem. Soc. 150 (2003) 1333.
- [11] J.N. Broughton, M.J. Brett, Electrochim. Acta 50 (2005) 4814.
- [12] J.K. Chang, W.T. Tsai, J. Electrochem. Soc. 152 (2005) 2063.
- [13] S. Devaraj, N. Munichandraiah, Electrochem. Solid State Lett. 8 (2005) 373.
- [14] M. Nakayama, T. Kanaya, R. Inoue, Electrochem. Commun. 9 (2007) 1154.
- [15] E.C. Rios, A.V. Rosario, R.M.Q. Mello, L. Micaroni, J. Power Sources 163 (2007) 1137.
- [16] A.E. Fischer, K.A. Pettigrew, D.R. Rolison, R.M. Stroud, J.W. Long, Nano Lett. 7 (2007) 281.
- [17] V. Subramanian, H.W. Zhu, R. Vajtai, P.M. Ajayan, B.Q. Wei, J. Phys. Chem. B 109 (2005) 20207.
- [18] M. Xu, L. Kong, W. Zhou, H. Li, J. Phys. Chem. C 111 (2007) 19141.
- [19] P. Soudan, J. Gaudet, D. Guay, D. Belanger, R. Schulz, Chem. Mater. 14 (2002) 1210.
- [20] T. Brousse, P.L. Taberna, O. Crosnier, R. Dugas, P. Guillemet, Y. Scudeller, Y.K. Zhou, F. Favier, D. Belanger, P. Simon, J. Power Sources 173 (2007) 633.
- [21] Y.C. Hsieh, K.T. Lee, Y.P. Lin, N.L. Wu, S.W. Donne, J. Power Sources 177 (2008) 660.
- [22] W.F. Wei, W.X. Chen, D.G. Ivey, J. Phys. Chem. C 111 (2007) 10398.
- [23] W.F. Wei, X.W. Cui, W.X. Chen, D.G. Ivey, J. Phys. Chem. C 112 (2008) 15075.
- [24] W.F. Wei, X.W. Cui, W.X. Chen, D.G. Ivey, Electrochim. Acta (2008), doi:10.1016/j.electacta.2008.10.031.
- [25] W.F. Wei, W.X. Chen, D.G. Ivey, Chem. Mater. 19 (2007) 2816.
- [26] M. Chigane, M. Ishikawa, J. Electrochem. Soc. 147 (2000) 2246.
- [27] B. Djurfors, J.N. Broughton, M.J. Brett, D.G. Ivey, Acta Mater. 53 (2005) 957.
- [28] M. Nakayama, A. Tanaka, Y. Sato, T. Tonosaki, K. Ogura, Langmuir 21 (2005) 5907.
- [29] M. Toupin, T. Brousse, D. Belanger, Chem. Mater. 16 (2004) 3184.
- [30] T. Brousse, M. Toupin, R. Dugas, L. Athouel, O. Crosnier, D. Belanger, J. Electrochem. Soc. 153 (2006) 2171.
- [31] Y. Dai, K. Wang, J.Y. Xie, Appl. Phys. Lett. 90 (2007) 104102.
- [32] L. Athouel, F. Moser, R. Dugas, O. Crosnier, D. Belanger, T. Brousse, J. Phys. Chem. C 112 (2008) 7270.
- [33] W. Sugimoto, H. Iwata, K. Yokoshima, Y. Murakami, Y. Takasu, J. Phys. Chem. B 109 (2005) 7330.
- [34] Y.R. Nian, H. Teng, J. Electrochem. Soc. 149 (2002) 1008.